Strain driven negative Poission's ratio and extraordinary light harvesting response of penta-BCN monolayer

Shambhu Bhandari Sharma*[a], Ram Chandra Bhatta[a], Rajendra Adhikari[b] and Durga Paudyal*[c,d]

[a]*Goldengate International College, Tribhuvan University, Kathmandu, Nepal*

[b]*Department of Physics, Kathmandu University, Dhulikhel, Kavre, Nepal*

[c]*Ames Laboratory, Iowa State University, Ames, IA 50011 , USA*

[d]*Electrical and Computer Engineering,and Computer Science Departments, Iowa State University, Ames, IA 50011, USA*

ARTICLE INFO

ABSTRACT

We report here, structural, dynamic, and mechanical stability in pentagonal boron carbon nitride (p-BCN) monolayer, a new member of direct bandgap two-dimensional (2D) semiconductor. The identified visible range bandgap with excellent mechanical strength allows it to be a promising candidate material in optoelectronics and nanomechanics. By employing density functional theory (DFT), we reveal a unique geometrical reconstruction with rigidity in B−N and C−N bond lengths with applied strain. These quasi-sp^3 hybridized short and strong covalent bonding and unique geometry support the monolayer to possess extraordinary mechanical response. Remarkably, the very rare, negative Poisson's ratio (NPR), with softening and hardening, mechanical anisotropy to isotropy is achieved with the application of a small value of strain. Similarly, the desired bandgap is manipulated by loading the biaxial strain. Most importantly, our predictions on p-BCN show excellent optical response such as good static dielectric constant and refractive index, strong optical absorption (up to 1.08×10^5 cm^{-1} in VR and 7.01×10^5 cm^{-1} in UV) with small energy loss and reflectance both appearing in visible and ultraviolet regions (UV). The desired optical response along with the blue and red shift is demonstrated by tailoring with tensile and compressive strain. Additionally, the predicted strong optical anisotropy provides it's application in polarized photodetection.

1. Introduction

Two-dimensional (2D) crystals are the blazing lights on the horizon of materials research due to their unique characteristics and intriguing applications [1, 2]. The stability and physical and chemical properties of these materials mainly depend on the lattice structure and atomic arrangement. For instance, the puckered, buckled, and planar arsenene show significantly different stability factors and electronic behavior from each other [3]. In addition, the planar indiene shows a metallic behavior contrasting with the semiconducting nature of buckled indiene [4].

In recent years a new class of 2D materials with pentagonal structure is drawing considerable attention due to their novel chemical and physical properties[5, 6, 7, 8, 9, 10]. The study of pentagonal 2D structures, similar to the Cairo pentagonal tiles, began when penta-graphene (PG), a five-membered rings of carbon atoms, was theoretically characterized [11]. The novel mechanical and electronic properties, and broad applications of penta-graphene inspired to explore more isostructures. Since then, tremendous efforts have been made to study the corresponding families of 2D materials both theoretically and experimentally. For example, penta-silicene nanoribbons [6, 12, 13], penta PdSe$_2$ [14, 15] are successfully fabricated by micromechanical exfoliation technique [5]. In addition, penta-germanium [7], penta-arsenic carbide [8], penta-CN$_2$ [10], penta-B$_2$C [9]

have been studied theoretically to investigate different physical and chemical properties. Interestingly, several studies show that penta-2D monolayer exhibits excellent chemical and physical properties, some of them are even better than hexagonal monolayer counterparts due to their unique puckered geometry. For example, penta-CN$_2$ exhibits higher energy density and greater in-plane stiffness than the h-BN monolayer [10].

Realizing the fact that there can be more degrees of freedom for physical and chemical properties, very recently, a new ternary pentagonal prototype, composed of B, N, and C atoms, pentagonal boron nitrogen carbide (p-BCN), has been theoretically predicted, which is mechanically, thermally, and dynamically stable direct bandgap semiconductor with excellent piezoelectric response [16]. These three abundant neighboring elements in the periodic table have an almost equivalent atomic size and mass, and lightweight are benign to the environment to form p-BCN exhibiting intrinsic polarization and piezoelectricity [16], and lattice thermal conductivity up to 97.49 Wm^{-1} K^{-1} at room temperature [32]. Moreover, the hydrogenation in pristine p-BCN changes it from a direct bandgap of 1.70 eV to an indirect bandgap of 4.46 eV. The bandgap of hydrogenated p-BCN is tuneable up to 3.26 eV under the biaxial strain. Although the elastic modulus tensor is reduced due to the hydrogenation, the spontaneous polarization is reported to be significantly enhanced [17].

The bandgap of p-BCN calculated by using Heyd-Scuseria-Ernzerhof (HSE) [18] hybrid functional within DFT is in the visible range. Because of that, it has great potential to be used in photocatalytic and optoelectronic

*Corresponding author
✉ shambhubhandari789@gmail.com (Shambhu Bhandari Sharma*); durga@ameslab.gov (D. Paudyal*)
ORCID(s):

devices [19, 20]. In addition, the buckled direct bandgap semiconductor is predicted to be an excellent optoelectronic material due to it's favorable surface for the photon-electron interaction [21]. What is lacking here is a meticulous study on optoelectronic properties. For applicability, it is crucial to test the mechanical stability, and strength as well as manipulate the optoelectronic behavior. Understanding the importance, we performed DFT calculations to investigate, reveal, and engineer the peculiar structural, mechanical, and optoelectronic properties of the p-BCN monolayer and analyze the influence of strain.

2. Computational Details

We have used DFT implemented in the Spanish initiative for electronic simulations with thousands of atoms (SIESTA) [22, 23] with norm-conserving pseudopotentials in the semilocal form [24]. The employed generalized gradient approximation (GGA) functional with Perdew-Burke-Ernzerhof (PBE) [25] treats underlying exchange and correlation within the double zeta plus polarization (DZP) basis sets. We have used 20×20×1 Monkhrost pack scheme [26] to perform Brillouin zone integration . The reciprocal space is expanded by using an energy cutoff of 350 Rydberg. The atomic relaxation is achieved when the force reached the value of 0.02 eV/Å using the standard conjugate-gradient (CG) technique. The convergence criteria for the energy of the self-consistent field is set to 1.0×10^{-6} eV. The vacuum gap of 25 Å is used along the z-direction to prevent unnecessary interactions between the adjacent unit cells. The chemical stability is achieved by calculating and analyzing the formation (E_f) [10] and cohesive (E_{coh})[27] energies.

$$E_{\mathrm{coh}} = \left(E - \sum_{i=\mathrm{B,C,N}} n_i E_i \right) / N \qquad (1)$$

$$E_f = E_{coh(p-BCN)} - x\mu_\mathrm{B} - y\mu_\mathrm{C} - z\mu_\mathrm{N} \qquad (2)$$

where, E represents the total energy of a monolayer and E_i represents the total energy of isolated atoms with n_i as the number of a specific atom per monolayer. $\mu_\mathrm{B}, \mu_\mathrm{C}$, and μ_N represent the chemical potential of respective atoms. The x, y and, z represent the number of B, C, and N atoms in unit cell, respectively. Further, we adopt the density-functional perturbation theory (DFPT) implemented in Quantum-Espresso package [28] for the calculations of the phonon dispersions of the monolayer. We obtain an accurate force matrix with $5 \times 5 \times 1$ supercell. For optical properties calculations, a denser k-point mesh, i.e. $60 \times 60 \times 1$, within the Monkhorst-Pack scheme and optical broadening of 0.1 eV is used. Optical calculations in SIESTA are based on the first order time dependent perturbation theory (TDP)[29]. The complex dielectric function ($\varepsilon(\omega)$) can be expressed as:

$$\varepsilon(\omega) = \varepsilon_1(\omega) + i\varepsilon_2(\omega) \qquad (3)$$

where $\varepsilon_2(\omega)$ is imaginary part of $\varepsilon(\omega)$ and can be obtained with the help of TDP [30]

$$\varepsilon_2(\omega) = \frac{e^2}{\omega^2 \pi m^2} \sum_{v,c} \int_{BZ} d\vec{k} \left| \langle \psi_{ck} | \hat{e} \cdot \vec{p} | \psi_{vk} \rangle \right|^2 \delta \left(E_c(k) - E_v(k) - \hbar\omega \right) \qquad (4)$$

Here, v and c represent the valence and the conduction band states, respectively. $E_{(c,v)}(k)$ and $\psi_{(c,v),k}$ are the corresponding energy and eigenfunction of these states. $\vec{p}$ and $\hat{e}$ are the momentum operator and polarization vector, respectively. The equation (4) displays the connection between optical and electronic properties. Further, real part of dielectric fuction $\varepsilon_1(\omega)$ is obtained by Kramer-Kronig transformation (KK) of $\varepsilon_2(\omega)$ and is expressed as:

$$\varepsilon_1(\omega) = 1 + \frac{2}{\pi} P \int_0^\infty \frac{\varepsilon_2(\omega')\,\omega'}{\omega'^2 - \omega^2} d\omega' \qquad (5)$$

where P denotes the principle part of $\varepsilon_1(\omega)$ [30].

Further, the complex refractive index (N) is expressed as $N = \sqrt{\varepsilon(\omega)} = \eta(\omega) + iK(\omega)$, where $\eta(\omega)$ and $K(\omega)$ are the refractive index and extinction coefficient, respectively. These parameters are expressed as:

$$\eta(\omega) = \left(\frac{\sqrt{\varepsilon_1^2(\omega) + \varepsilon_2^2(\omega)} + \varepsilon_1(\omega)}{2} \right)^{\frac{1}{2}} \qquad (6)$$

$$K(\omega) = \left(\frac{\sqrt{\varepsilon_1^2(\omega) + \varepsilon_2^2(\omega)} - \varepsilon_1(\omega)}{2} \right)^{\frac{1}{2}} \qquad (7)$$

Further, the reflectivity, R(ω) and absorption coefficient, $\alpha(\omega)$ are expressed as [31]:

$$R(\omega) = \frac{K(\omega)^2 + [1 - n(\omega)]^2}{K(\omega)^2 + [1 + n(\omega)]^2} \qquad (8)$$

$$\alpha(\omega) = \frac{2\omega K(\omega)}{c} \qquad (9)$$

Additionally, the electron energy loss function, L(ω) is given by the relation $L(\omega) = \mathrm{Im}\left(-\frac{1}{\varepsilon(\omega)} \right)$ and also in terms of $\varepsilon_1(\omega)$ and $\varepsilon_2(\omega)$,

$$L(\omega) = \frac{\varepsilon_2(\omega)}{\varepsilon_1(\omega)^2 + \varepsilon_2(\omega)^2} \qquad (10)$$

All these optical parameters are calculated in the interval between 0 to 20 eV for parallel (E∥x) polarization of electric field.

3. Results and Discussions

3.1. Structural properties and influence of strain

The optimized unit cell of p-BCN consists of six atoms (2B, 2N, and 2C), with a B/C/N ratio of 1:1:1, forming a pentagonal 3 layered 2D monolayer. The first, second, and third layers consist of B (or N), purely C, and N (or B) atoms inside a rectangular cell, respectively. This monolayer belongs to C_2^2 symmetry (space group 4) in the pentagonal crystal family. The fully relaxed structure (Fig.1) consists of lattice constants a=3.69 Å and b=3.66 Å, which fairly agree with previous reports [16, 32]. Expanding the unit cell into a larger supercell, one can see four distinct irregular pentagonal Cairo tiles (labeled by I−IV in Fig. 1), having different bond lengths and bond angles between atoms. We consider two C atoms located in different positions form different bond angles and bond lengths with other atoms. We mark the positions of these two atoms as C1 and C2 in the unit cell to remove the obscure visualization. Although the previous report has not shown this fact, here, we have presented the detailed bond analysis (Table 1). The bond length plays a direct role in the stability and physical and chemical properties. The shorter bond length allows to have stronger structure. Comparatively, the B−N (1.43 Å) is the shortest and strongest quasi-sp³ hybridized bond. This particular bond in p-BCN is even shorter than in the h-BN monolayer (1.45 [33]). Moreover, the thickness of the p-BCN monolayer, calculated by subtracting the topmost and lowermost vertical positioning of atoms, is 1.36 Å. This thickness is larger than other 2D penta structures [34, 35, 36] including the penta- graphene (1.20 Å[11]) but lesser than those of penta-BP$_5$ (2.50 Å[37]) and penta-CN$_2$ (1.52 Å[10]).

Since the structural stability and nature of chemical bonds are closely related, we analyze Mulliken charge density to understand the bonding mechanism. There is a clear display of surface charge distribution index in the monolayer (Fig.2(f)). The red and blue colors represent the lowest and highest electron density regions, respectively. Both the iso-surface charge distribution and 2D valence charge contour plots confirm the higher charge distribution around nitrogen atom as compared to other atoms. This also elucidates the highest ionization energy of nitrogen as appeared in h-BN monolayer[33]. The careful charge density analysis shows that there is a considerable overlap of electronic wave functions due to shared electrons between B and N. Such a directional bond indicates the presence of co-valent bonding in good agreement with previous report[16]. A similar configuration between C and B atoms indicates the covalent nature of bonding. The iso-surface (Fig. 2(a)), which displays the charge sharing between B and C, and B and N atoms, also supports this fact. On the other hand, the deformed dumb-bell shapes of counter lines around the N and C atoms indicate the sharing and transferring of charges suggesting the partly ionic and covalent bonding.

The chemical stability is confirmed by calculating the cohesive energy (-5.68 eV/atom) using Eqn. 1. This large
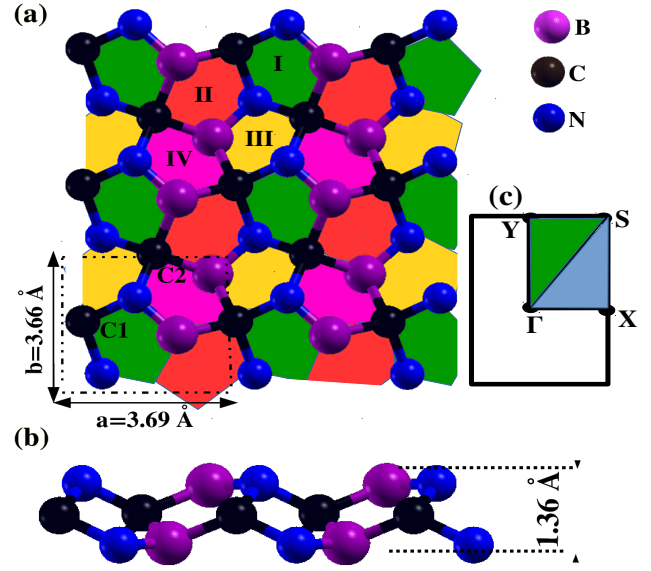

Figure 1: (Color online) Optimized structure ($3 \times 3 \times 1$ supercell) of p-BCN monolayer showing Cairo pentagonal geometry (a) top view and (b) side view (c) Schematic diagram of high-symmetry path in the first Brillouin zone. The unit cell is indicated by doted line.
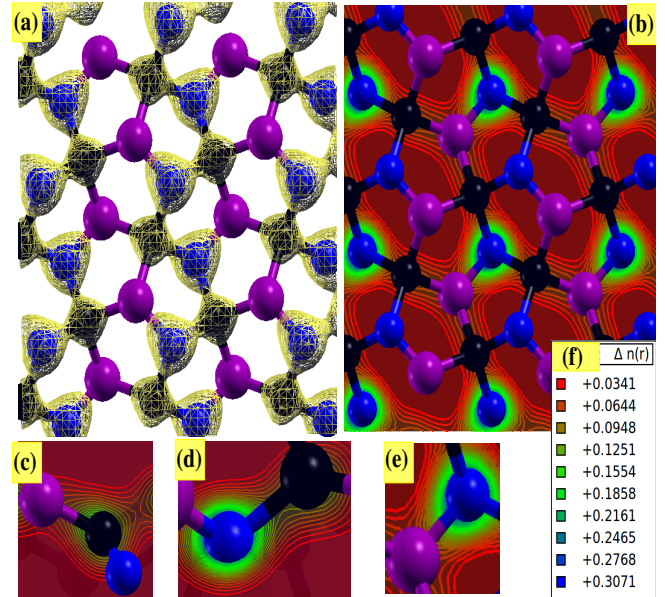

Figure 2: (Color online) Valence charge density contour with (a) charge isosurface, (b-f) charge distribution between the bonding atoms at 0.05 eV/Å for p-BCN monolayer.

negative value of cohesive energy suggests that p-BCN is a stable monolayer. Additionally, the calculated formation energy (Eqn. 2) (E_f) is -2.07 eV/atom thereby confirming the feasibility of it's experimental synthesis. The dynamical stability is calculated by phonon band dispersion (Fig. 3). The presence of only a non-imaginary band ensures the dynamic stability of the p-BCN monolayer.
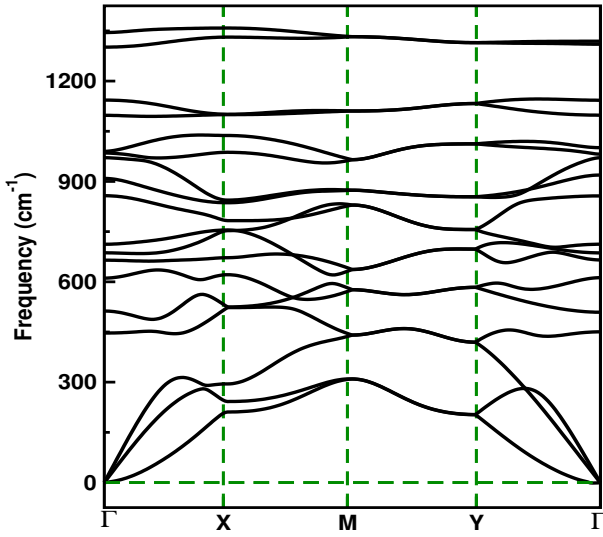
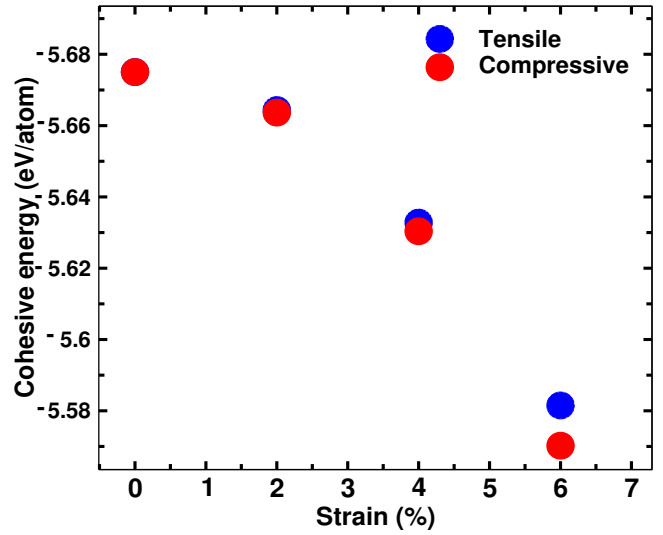**Figure 3:** (Color online) Phonon band dispersion diagram for p-BCN monolayer.

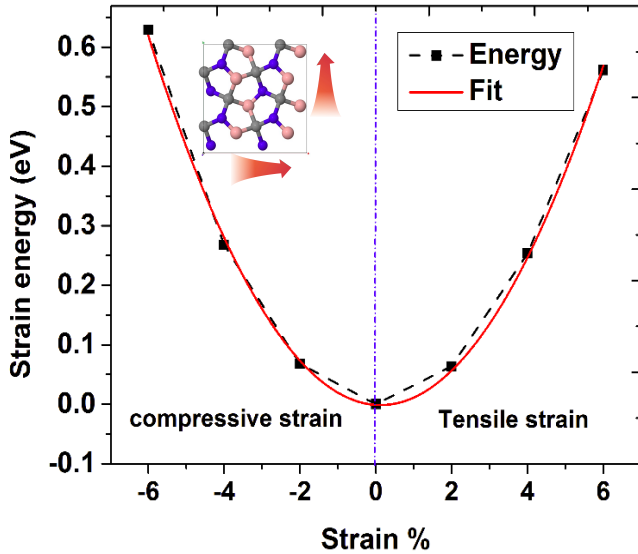**Figure 5:** (Color online) The cohesive energy as a function of strain.

Figure 4: (Color online) The strain energy versus compressive and tensile equi-biaxial strain profile for p-BCN monolayer.

system is the most stable. The magnitude of cohesive energy decreases slightly while applying the strain.

The bond length between each atoms increases (decreases) with increasing tensile (compressive) biaxial strain (Fig. 6). However, the rate of variation is less in the B−N bonds as compared to other bonds. This result is attributed to the shorter bond length with stronger inter-atomic interaction and quasi-sp^3 hybridized covalent bonding between the B and N atoms. The C1− N bond also varies slowly showing it's rigidity toward the strain. Similarly, the bond angle between C1−N−C2, B−N−C1, B−N−C2, also increases monotonically with the increase in strain (Fig. 7). However, the bond angle between B−C1−N, N−C1−N decreases in the same fashion. This reduction is due to the geometrical positioning and re-arrangement of atoms by strain. Similarly, the thickness (h) decreases monotonically with the applied tensile strain. It suggests that the material tends to extend horizontally and compress vertically. This is analogous to stretching the dough and it's relative deformation. Thus, it is clear from the analysis that a geometrical deformation is created due to the applied strain.
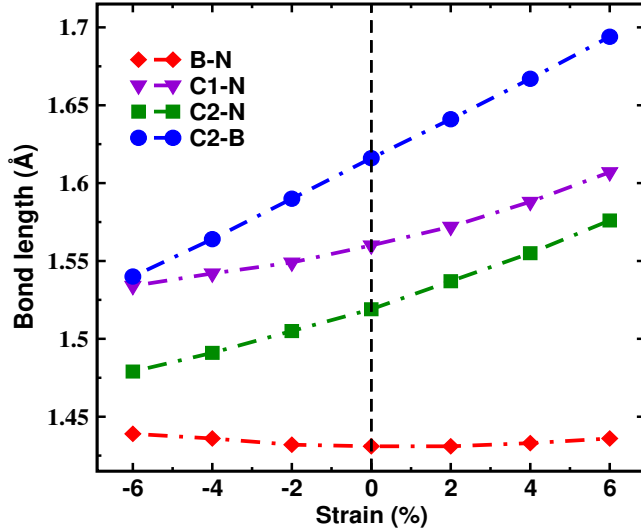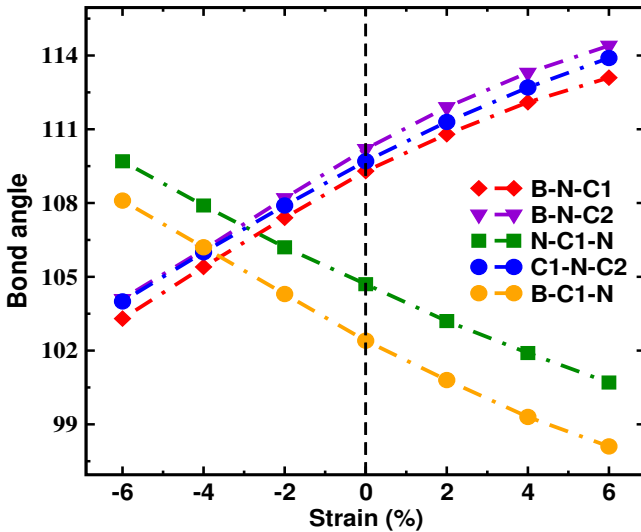
3.2. Influence of strain in mechanical properties

The mechanical strength and stability of p-BCN is investigated by calculating second order elastic constants (stiffness tensor) C_{ij} using the finite distortion method [39]. For this particular crystal symmetry, C_{11}, C_{22}, C_{12} and C_{66} are only the significant independent elastic stiffness constants. These constants are further used to investigate the mechanical strength criteria [40]: $C_{11}C_{22} − C_{11}^2 > 0$ and $C_{66} > 0$. Similarly, the 2D Young's modulus in (100) and (010) directions (Ya and Yb) is calculated by $Y_a = \left(C_{11}^2 − C_{12}^2\right)/C_{11}$, $Y_b = \left(C_{22}^2 − C_{12}^2\right)/C_{11}$. The shear modulus (G) is nothing but the value of C_{66}. In addition, the Poisson's ratio in (100) and (010) directions (ϑ_a and ϑ_b) is calculated by $\vartheta_a = C_{12}/C_{11}$ and $\vartheta_b = C_{12}/C_{22}$.

After confirming the equilibrium structural properties of p-BCN, it's crucial to test the structural properties at different strain conditions because the strain is unavoidable in material growth and processing [38]. The biaxial strain (ε) is applied within the harmonic range -6% to 6% at the step of 2% by varying a and b at an equal rate. The strain versus strain energy (Fig. 4) profile demonstrates the range of compressive and tensile equi-biaxial strain. For each iteration of strain, the atomic positions are fully optimized to make favorable arrangements of atoms. The monolayer is chemically stable within this range which is illustrated by calculating the cohesive energy (Fig. 5) at each value of strain. These calculations indeed confirm that the strain-free

Table 1
Structural properties: bond lengths and bond angles.

	Bond (lengths) (Å)					Bond angles (degree)				
S.N	$B-N$	$C1-N$	$C2-N$	$C2-B$	h	$\angle B-N-C1$	$\angle B-N-C2$	$\angle N-C1-N$	$\angle C1-N-C2$	$\angle B-C1-N$
p-BCN	1.43	1.52	1.56	1.62	1.36	110.2	109.3	104.7	109.7	102.04
Ref. [16]	1.41	1.51	–	1.62	1.34	–	–	–	–	–

Figure 6: (Color online) Variation of bondlength in p-BNC with applied biaxial strain.

Figure 7: (Color online) Variation of bond angle in p-BCN with applied biaxial strain.

Further, the mechanical anisotropy is tested by calculating Li's elastic anisotropy measurement methods [41]. In particular, we investigate the universal A^{SU}, Ranganathan $A^{Ranganathan}$ [42], and Kube A^{Kube} [43] anisotropy indices which is sufficient enough to measure mechanical anisotropy. For this, the Voigt and Reuss estimated area (K^V and K^R) and shear moduli (G^V and G^R) are calculated using

the following formula [41]:

$$K^{V} = \frac{C_{11} + C_{22} + 2C_{12}}{4},$$
$$G^{V} = \frac{C_{11} + C_{22} - 2C_{12} + 4C_{66}}{8},$$
$$K^{R} = \frac{1}{S_{11} + S_{22} + 2S_{12}},$$
$$G^{R} = \frac{2}{S_{11} + S_{22} - 2S_{12} + S_{66}},$$

(11)

where S_{ij} are the the compliance matrix equivalent to reciprocal of C_{ij} matrix [41].

Furthermore, other mechanical anisotropy indices are calculated as follow:

$$A^{SU} = \left(\begin{array}{c} \left[\frac{1}{4}\left(C_{11} + C_{22} + 2C_{12}\right)\left(S_{11} + S_{22} + 2S_{12}\right) - 1\right]^{2} \\ +2\left[\frac{1}{16}\left(C_{11} + C_{22} - 2C_{12} + 4C_{66}\right)\right. \\ \left. \left(S_{11} + S_{22} - 2S_{12} + S_{66}\right)^{2}\right] \end{array} \right)^{\frac{1}{2}},$$

$$A^{Ranganathan} = \frac{K^{V}}{K^{R}} + 2\frac{G^{V}}{G^{R}} - 3 \geq 0, \quad (12)$$

$$A^{Kube} = \sqrt{\left(\ln \frac{K^{V}}{K^{R}}\right)^{2} + 2\left(\ln \frac{G^{V}}{G^{R}}\right)^{2}}, \quad (13)$$

Further, for the better visualization of anisotropy, Young's and shear modulii, and Poisson's ratio ϑ are also calculated as a function of the direction angles θ [44]:

$$E(\theta) = \frac{C_{11}C_{22} - C_{12}^{2}}{C_{22}\cos^{4}(\theta) + A\cos^{2}(\theta)\sin^{2}(\theta) + C_{11}\cos^{4}(\theta)}$$

$$\vartheta(\theta) = \frac{C_{12}\cos^{4}(\theta) - B\cos^{2}(\theta)\sin^{2}(\theta) + C_{12}\cos^{4}(\theta)}{C_{22}\cos^{4}(\theta) + A\cos^{2}(\theta)\sin^{2}(\theta) + C_{11}\cos^{4}(\theta)}$$

$$\frac{1}{G(\theta)} = \left[S_{11} + S_{22} - S_{12}\right]\cos^{2}(\theta)\sin^{2}(\theta) + \frac{1}{4}S_{66}\left[\cos^{4}(\theta) + \sin^{4}(\theta) - 2\sin^{2}(\theta)\cos^{2}(\theta)\right]$$

(14)

where $A = \left(C_{11}C_{22} - C_{12}^{2}\right)/C_{66} - 2C_{12}$ and
$B = C_{11} + C_{22} - \left(C_{11}C_{22} - C_{12}^{2}\right)/C_{66}$,

Table 2

The calculated elastic constants C_{ij}, 2D Young's modulus Y, Poisson's ratio ϑ, and shear modulus G, and mechanical stability condition of p-BCN monolayer

| Strain% | C_{ij} (N/m) | | | | Y(N/m) | | G(N/m) | $\vartheta(N/m)$ | | Stability |
	C_{11}	C_{22}	C_{12}	C_{66}	Y_a	Y_b	G_{xy}	ϑ_a	ϑ_b	Yes/No
6	172.43	164.77	-7.72	90.08	172.07	164.42	90.08	-0.045	-0.047	Yes
4	189.46	176.43	-8.39	98.92	189.062	176.06	98.926	-0.044	-0.048	Yes
2	201.88	178.34	-5.02	103.45	201.74	178.21	103.45	-0.025	-0.028	Yes
0	210.15	170.77	4.27	102.93	210.05	170.66	102.93	0.020	0.025	Yes
Ref[32]	214.45	176.10	4.38	103.54	214.36	175.99	-	0.020	0.025	Yes
Ref[16]	223.56	189.16	4.90	104.80	223.45	189.03	-	0.022	0.026	Yes
-2	205.25	145.97	21.75	91.74	202.01	143.6	91.74	0.106	0.149	Yes
-4	231.73	149.68	48.54	91.59	215.99	139.51	91.59	0.209	0.324	Yes
-6	440.72	340.78	391.73	24.49	-	-	-	-	-	No

With this analysis, we confirm the mechanical stability by calculating the values of C_{ij} tensors (Table 2) and fitting with mechanical criteria [40]. The calculated Young's moduli ($Y_a = 210.047$ N/m, and $Y_b = 170.669$ N/m), Poisson's ratio ($\vartheta_a = 0.025$, $\vartheta_b = 0.020$), and shear modulus (G_{xy}=102.93 N/m) are very consistent with available literature [16, 32].

Further, introducing the strain, mechanical response (Table 2) and elastic anisotropy are calculated (Table 3). Surprisingly, 6% of compressive strain is mechanically unstable. This suggests that the material is not machineable and hard to operate for any applications at this strain. Compressing the monolayer at 2%, the Young's and shear moduli decrease, however, Poisson's ratio increases abruptly up to 0.149, which is indeed comparable to that of graphene [45], the strongest 2D material till now. This abrupt growth of Poisson'ratio continues up to 0.324 at 4% strain indicating the ductile behavior. This fact is also supported by the maximum value (215.99) of Y_a. In addition, the anisotropy indices (Table 3) describe the elastic anisotropic behavior of the monolayer. The zero value of anisotropy indices refers to the isotropic elastic response. Any change from that reference value indicates the degree of anisotropy. With the compressive strain, the indices, A^{SU}, $A^{Ranganathan}$, A^{Kube} shift to higher values indicating the increment in anisotropy. This fact is visualized by the polar plots (Fig. 8), in which the curves of Young and shear moduli, and Poisson's ratio gradually deform with the increase in compressive strain. The highest values of Young's modulus, Poisson's ratio, and shear modulus for the strain-free monolayer are located along the (100) (0°), (110) (45°), and (010) (90°), respectively, while minimum values are at (010) (90°), (010) (90°), and (110) (45°), respectively. This result is in good agreement with available literature [16, 32]. These maxima and minima fluctuate to different values with strain (Fig. 8).

On the other hand, loading tensile strain up to 6%, the monolayer shows consistent mechanical stability. Remarkably, from 2% of strain, the negative Poisson's ratio (NPR) is noticed with a monotonic reduction in Young's and shear moduli. The monolayer softens (Y=172 N/m) and possesses the largest value of NPR (-0.047) at 6% of strain. The early signature of negative Poisson's ratio is indicated by rigidity in B−N and C1−N bonds (Fig. 6) and consistency in cohesive energy (Fig. 5) with applied strain. These basic requirements support the occurrence of NPR [46]. However, more advanced testing can be done [46]. The NPR behavior is very rare in 2D materials. Materials possessing such behavior are often called auxetic materials or mechanical metamaterials, which are very important in multiple applications such as tension activatable substrates, nanoauxetic materials, deformable variable stiffness materials [11]. The NPR is also reported in strain-free penta graphene [11] indicating the broad application of this behavior. Converse to compressive strain, the anisotropy indices, A^{SU}, $A^{Ranganathan}$, and A^{Kube}, approach to smaller values indicating the reduction in anisotropy. At 6% of strain, the monolayer shows a highly elastically isotropic response. This fact is visualized by the polar plots (Fig. 8), in which the curves of Young and Shear moduli, and Poisson's ratio gradually approach to be a perfect circle, indicating the anisotropy to isotropy transformation of the monolayer, with the increase in tensile strain. Therefore, diverse and unique mechanical behaviors are unraveled in p-BCN monolayer with the application of strain, which is in broad interest scientifically and technologically [47].

3.3. Electronic properties and influence of strain

To get insight into the electronic behavior of the p-BCN monolayer, we calculate the spin-polarized electronic band structure and partial density of states (PDOS). The electronic band structure is considered along the Γ - X - M - Y - Γ high-symmetry directions (Fig. 1c) in the first Brillouin Zone (BZ). The symmetry in spin up and spin down band structure (Fig. 9) and PDOS (Fig. 10) shows the
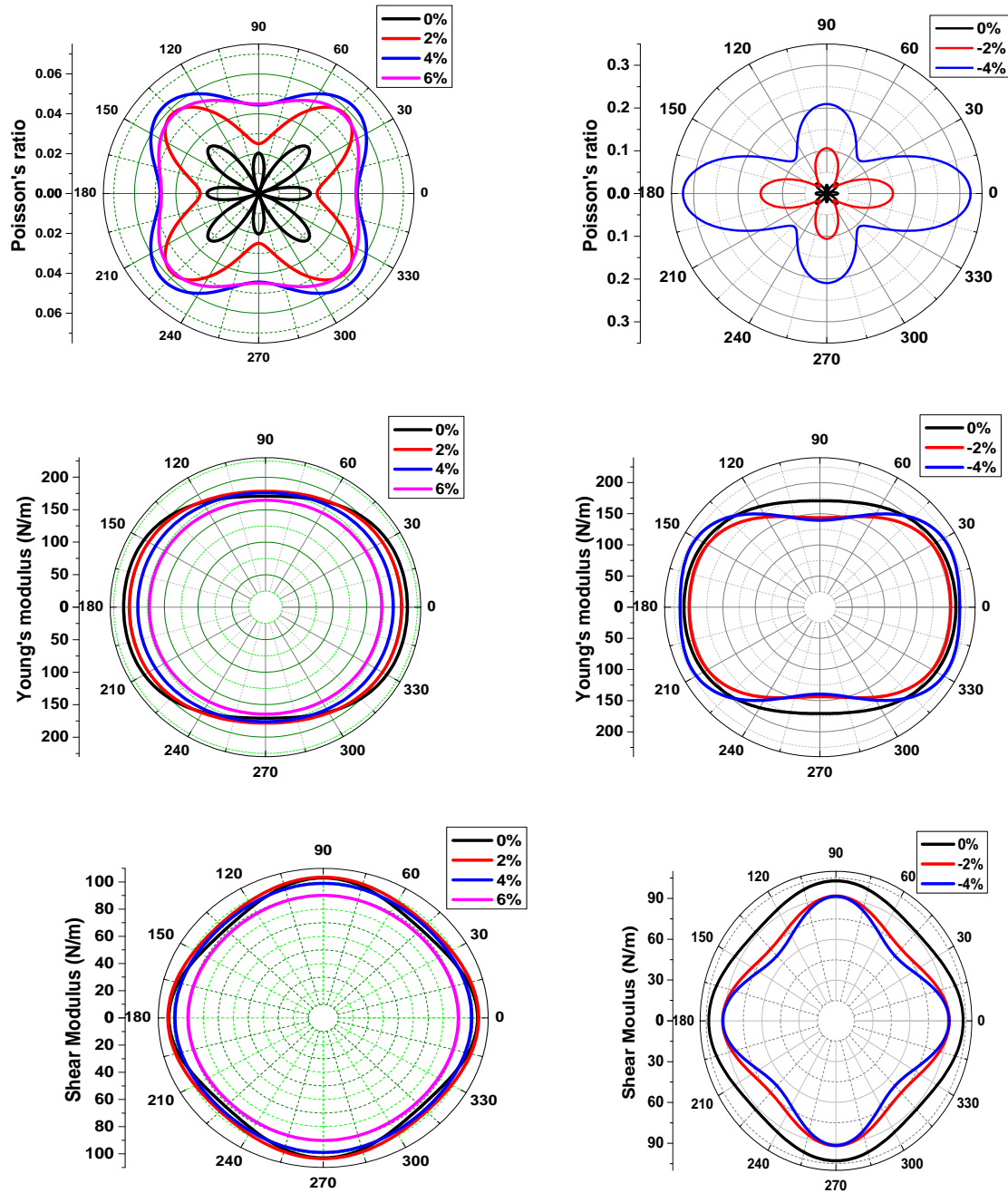
Figure 8: (Color online) The orientation dependent 2D Poisson's ratio, Young's modulus and, shear modulus for p-BCN under different compressive and tensile strains.

Table 3

Elastic anisotropy indices with applied strain, together with the Voigt and Reuss estimated area (K^V, K^R) and shear (G^V, G^R) moduli for p-BCN monolayer.

Strain (%)	G^V	G^R	K^V	K^R	A^{SU}	$A^{Ranganathan}$	A^{Kube}
6	89.123	89.095	80.438	80.392	0.0005	0.0012	0.0003
4	97.297	97.210	87.278	87.161	0.0013	0.0031	0.0008
2	100.515	100.231	92.543	92.183	0.0040	0.0096	0.0024
0	98.01	97.21	97.36	96.32	0.0116	0.0273	0.0069
-2	84.338	82.352	98.687	95.831	0.0341	0.0780	0.0194
-4	81.341	77.770	119.624	113.688	0.0649	0.1441	0.0353

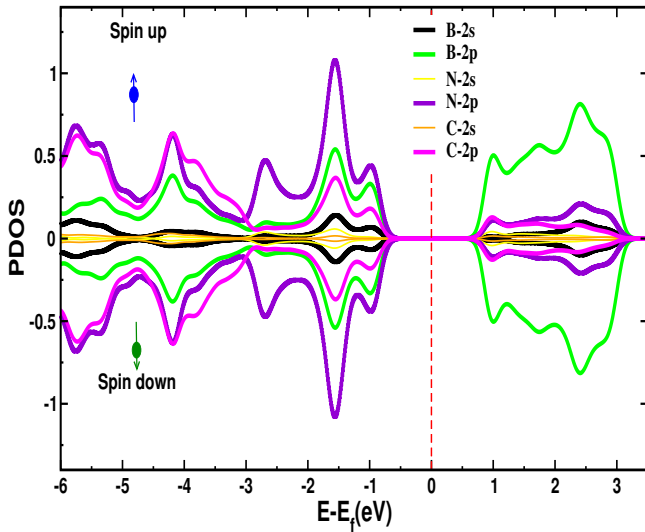**Figure 9:** (Color online) The electronic band structure of p-BCN for spin up and spin down states.

Figure 11: (Color online) Variation of TDOS with strain for p-BCN monolayer

Figure 10: (Color online) The spin-polarized partial density of states (PDOS) of p-BCN monolayer.

Figure 12: (Color online) Variation of bandgap as a function of strain in p-BNC. The Fermi level is shifted at the zero energy as represented by the horizontal red dashed line.

non mangnetic nature. This fact is also supported by the zero total magnetic moment.

The valence band maximum (VBM) and conduction band minimum (CBM) is located between the Γ - X path of the BZ (Fig.9) implying p-BCN as a direct bandgap semiconductor. The calculated direct bandgap using PBE is 1.77 eV, which is in good agreement with the previous reports[16, 32]. Furthermore, to understand the contribution of individual atomic orbital, the PDOS is plotted alongside the band structure. The plotted PDOS shows that N-2p and B-2p orbitals mainly contribute to the VBM and CBM, respectively, in good agreement with the available literature[48]. B−2s has minor contribution to VBM. Intrestingly, C−2p contributes to both VBM and CBM. This indeed allows us to distinguish it from h-BN [33].

Further, we applied equi-biaxial strain within the harmonic range to understand the electronic response. The
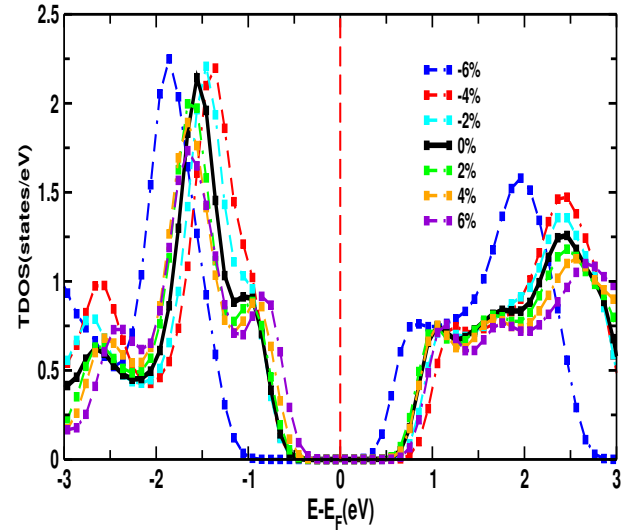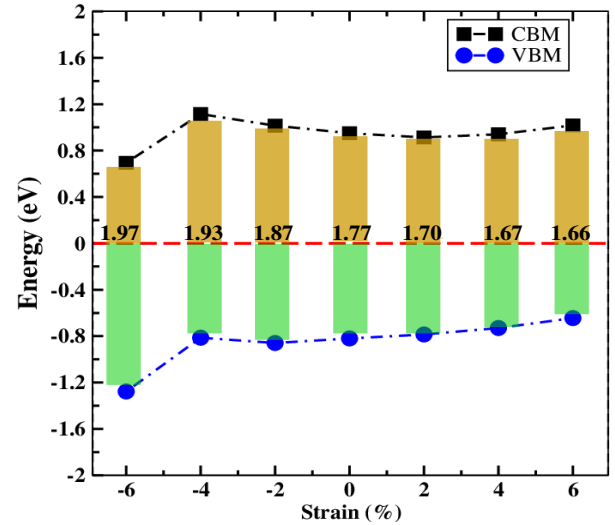
bandgap increases (decreases) monotonically with compressive (tensile) strain (Fig. 13). The values of bandgap with different strains are illustrated in Fig. 12. Interestingly, at or beyond 2% compressive strain, the equilibrium bandgap shifts from direct to indirect. The shift is the largest when compressive strain reaches 6%. The bandgap becomes 1.97 eV from 1.77 eV at this compressive strain. On the other hand, the bandgap reaches to 1.68 eV from 1.77 eV at the same value of tensile strain. This increment is 6.2% from the strain-free bandgap while the increment is 11.2% with compressive strain, which is twice the decreasing rate. Unlike the tensile strain, the direct bandgap has not shifted too noticeably in the compressive strain. Additionally, the VBM and CBM become constant after 4% tensile strain indicating the consistency in the bandgap. However, the VBM
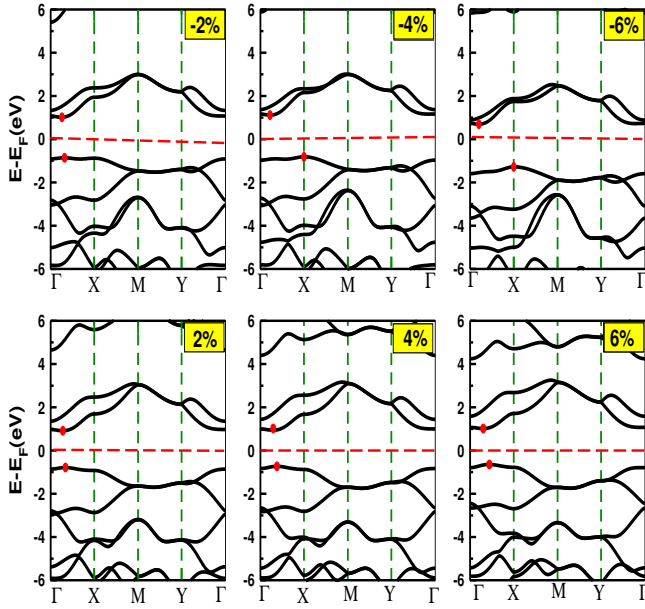
Figure 13: (Color online) Variation of electronic bands with tensile and compressive strain.

gradually shifts toward the Fermi-level with an increase in tensile strain. It is worth mentioning that a similar result of band tailoring is reported in a very recent study [32].

Further, the change of bandgap is illustrated from the total density of states (TDOS) at the same regime of strain (Fig. 11). The highest energy states shift toward the Fermi level reducing the bandgap. The change in bandgap is attributed to the degree of repulsion of electrons in atomic orbitals and delocalization effect due to the applied strain [49, 50, 51].

3.4. Optical properties and influence of strain

After making a good understanding of electronic band structure, which is inherently connected to the optical behavior of a semiconductor (Equ. 4), it is interesting to discuss the optical behavior of p-BCN. The optical response is calculated with the photon energy range of 0 eV to 20 eV. The incident polarized light is considered in in-plane (E∥x), and out-of-plane (E∥z) directions, which are sufficient directions to describe the optical behavior of this 2D system. We have performed spin non-polarized calculations to investigate the important optical parameters such as the real ($\varepsilon_1(\omega)$) and imaginary ($\varepsilon_2(\omega)$) parts of dielectric functions, absorption coefficient ($\alpha(\omega)$), electron energy loss function (ELF) ($L(\omega)$), refractive index ($\eta(\omega)$), and reflectivity ($R(\omega)$). To make a comparison, we plot these optical parameters side by side (Fig. 14) for both directions. It is well known that the optical response is determined by the amplitude and number of peaks in the optical response curves. Higher amplitude with a larger number of peaks in the in-plane direction demonstrates that the optical response of this monolayer is significantly better in E∥x than in E∥z. This optical anisotropy is attributed to the structural anisotropy of this monolayer. Considering

this, we limit our optical calculations for in-plane direction only. Furthermore, we apply biaxial strain and calculate the optical responses to compare with the calculated strain-free value.

The real part of the dielectric function (ε_1 (w)) is related to the energy stored by the medium when a material is exposed to an electromagnetic spectrum. Figure 15 depicts the calculated $\varepsilon_1(\omega)$ as a function of energy for the p-BCN monolayer at strain-free and strain applied conditions. For strain-free monolayer, two sharp peaks are located at VR (1.62 eV-3.23 eV or 360 nm-740 nm) while multiple peaks in the UV region ultimately become steady beyond 16 eV. After compressing and stretching, the intensity of peaks increases slightly anyway. This unusual result is described by the Penn model, which is also observed in an earlier report [52]. This phenomenon is also attributed to the geometrical re-arrangement of the pentagonal 2D system. Additionally, the value of $\varepsilon_1(\omega)$ is positive throughout the whole range of photon energy in both strained and strain-free conditions. The absence of negative $\varepsilon_1(\omega)$ confirms that there is no plasma frequency, the negative value of $\varepsilon_1(\omega)$, indicating the persistent semiconducting behavior of monolayer. Furthermore, the value of $\varepsilon_1(\omega)$ at zero photon energy, which corresponds to the static dielectric function $\varepsilon_1(0)$, is 2.04 at equilibrium condition. The static dielectric constant value of p-BNC monolayer is very close to that value of penta-graphene [53] but smaller than that of well-known 2D materials [54] including h-BN [55] for E∥x. However, this value slightly changes with applied strain. Interestingly, at 6% of compressive (tensile) strain, it reaches up to 2.14 (2.08) thereby alerting the fact that p-BCN is mechanically unstable at 6% of compression.

Moreover, the major optical behavior of a material is linked with the imaginary part of dielectric function ($\varepsilon_2(\omega)$) (Eqns. (3-8)). The $\varepsilon_2(\omega)$ describes the inter-band transitions by analyzing the major peaks. All the optical interband transitions are essentially due to the *p* orbitals of B, C, and N atoms which can be described by analyzing PDOS (Fig. 10). The two major sharper peaks, which arise at 1.90 *eV* and 2.90 *eV* for unstrained p-BCN in the VR region, justify the first inter-band transitions. In addition, multiple intense peaks are noticed in the UV region, whose intensity is oscillatory with strain. The amplitude of these peaks inappreciably increases (decreases) gradually with increasing tensile (compressive) strain. However, the rate of increment of the intensity of peaks in tensile strain is more than the rate of reduction in compressive strain. These results suggest that multiple rigorous inter-band transitions are created for UV and VR regions. Therefore, the p-BCN monolayer is an optically preferable material for both VR and UV-operated device applications.

Furthermore, the electron loss function (ELF) describes the amount of energy loss and collective excitation of electrons in a material when exposed to light. Noticeably, first, two sharper ELF peaks appear at 1.92 eV and 3.11 eV of the VR region. Multiple more intense peaks also appear in higher energy of UV indicating the more energy drop.
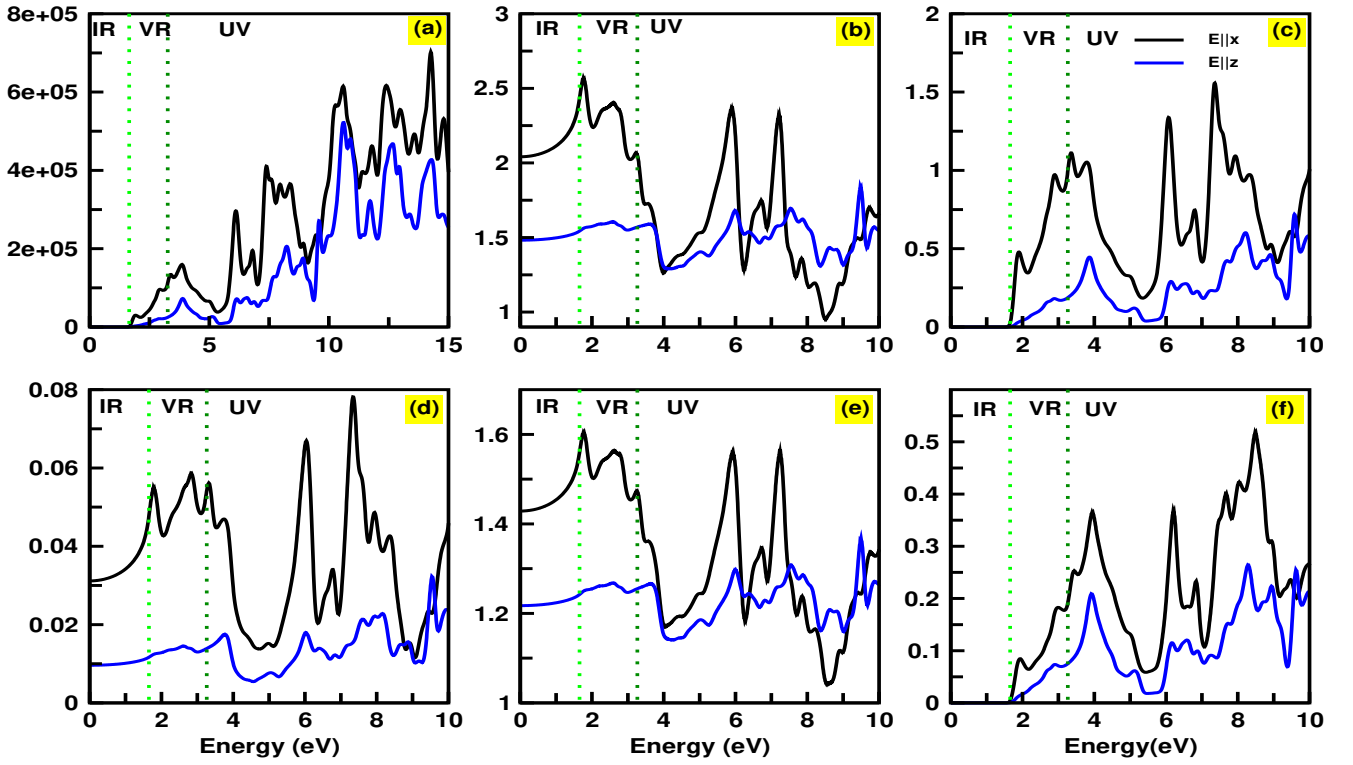
Figure 14: (Color online) (a) Absorption coefficient, (b) Real part of dielectric function, (c) Imaginary part of dielectric fuction, (d) Reflectance, (e) Refractive index, and (f) electron loss function, as a function of photon energy. Black and blue solid curves represent in-plane and out-plane incident light in p-BCN monolayer, respectively.
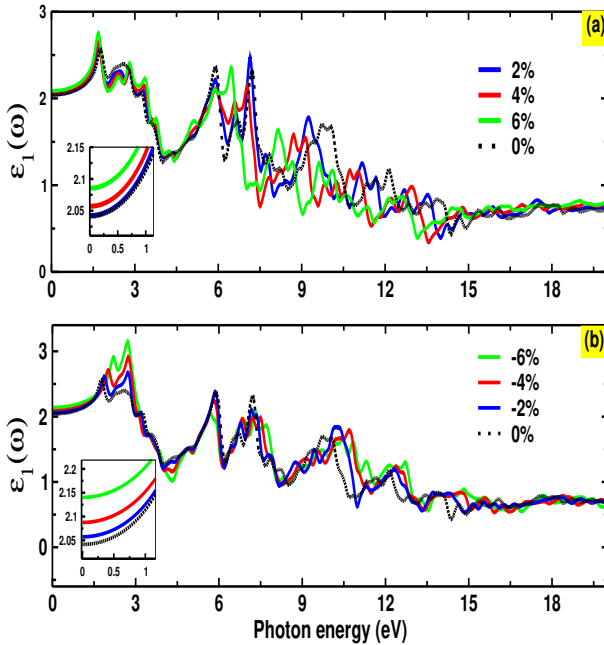

Figure 15: (Color online) Real part of dielectric function of p-BCN in tensile (a) and compressive (b) strain. The magnified view of $\varepsilon(0)$ is shown in inset.
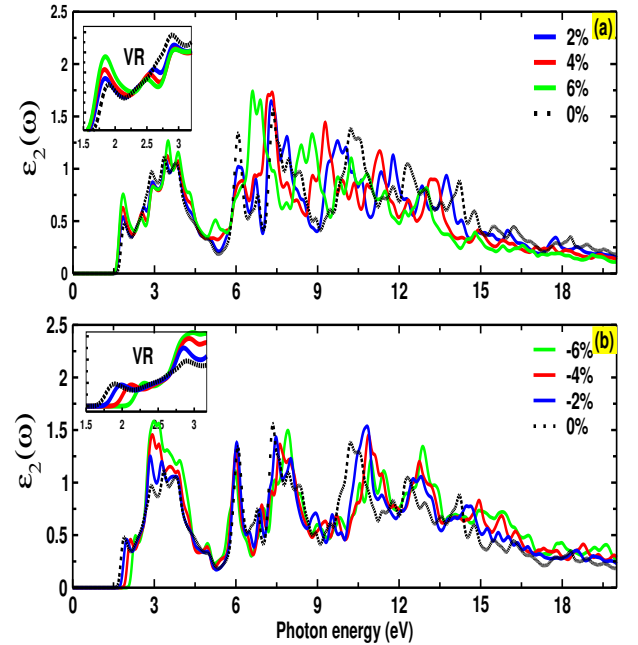

Figure 16: (Color online) Imaginary parts of dielectric function of p-BCN in tensile (a) and compressive (b) strain. The magnified view of VR region is shown in inset.

However, the magnitude of ELF is still very small as compared to PG [56], indicating low energy loss, suitable for energy harvesters. After introducing the strain, the amplitude of ELF peaks slightly increases (decreases) with tensile (compressive) strain. The threshold energy value of ELF
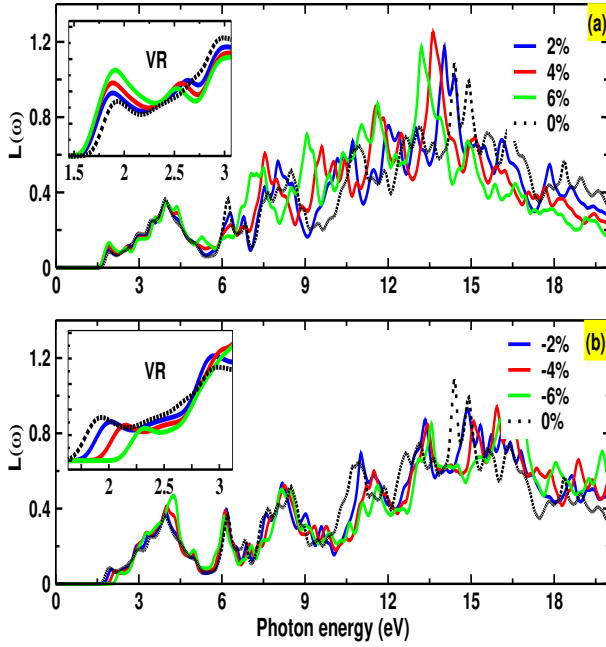
Figure 17: (Color online) Electron energy loss function (ELF) of p-BCN in tensile (a) and compressive (b) strain. The magnified view of VR region is shown in inset.
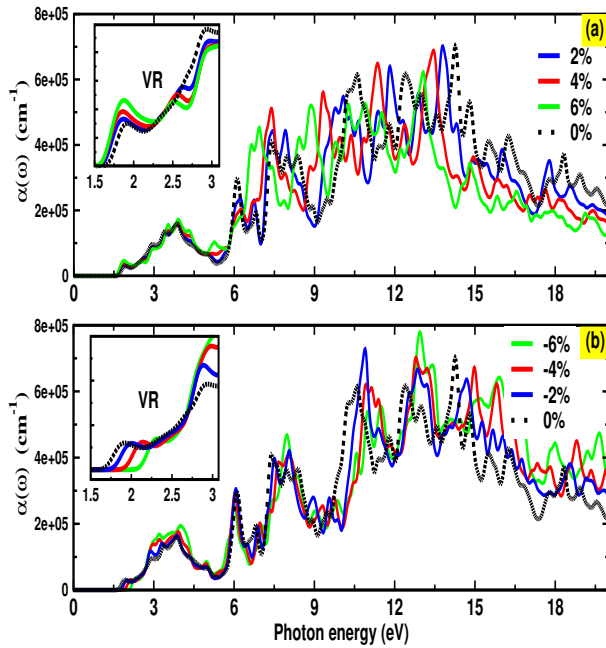

Figure 18: (Color online) Absorption coefficient of p-BCN in tensile (a) and compressive (b) strain. The magnified view of VR region is shown in inset.

shifts to a lower (higher) range with tensile (compressive) strain indicating the red shift and blue shift phenomena, respectively. These peaks have resulted from the oscillation of electric dipoles and the environment of ionization [57].

Similarly, the absorption coefficient ($\alpha(\omega)$) and reflectivity ($R(\omega)$) are closely related with $\varepsilon_2(\omega)$ as described in equations (3-8). The direct relationship between optical
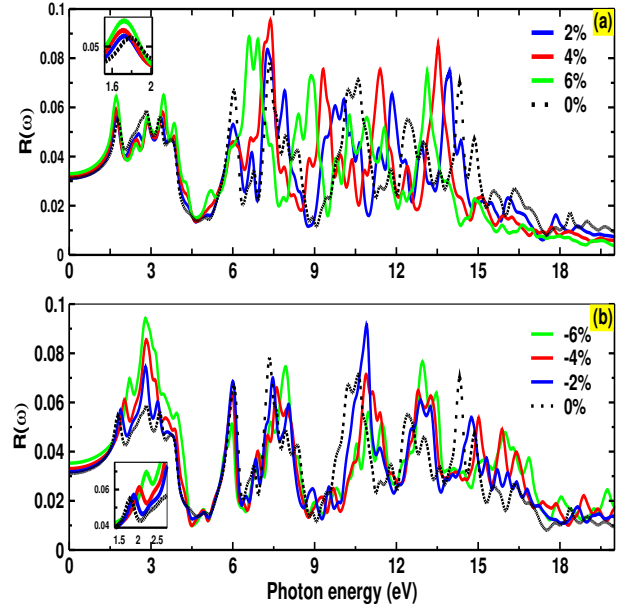

Figure 19: (Color online) Reflectivity of p-BCN in tensile (a) and compressive (b) strain. The magnified view of VR region is shown in inset.

absorption coefficient and dielectric function is illustrated in Fig. 16 & Fig. 18. The threshold value of energy in $\alpha(\omega)$ to excite the peaks is known as absorption edge (A_e). The absorption edge is approximately at 1.69 eV which is equivalent to electronic bandgap (1.77 eV) suggesting the direct transition of photo-excited electrons from the VBM to the CBM. However, this value increases with compressive strain and reaches 1.83 eV at 6% (blue-shift). In contrast, the absorption edge decreases with increasing tensile strain and reaches 1.30 eV at 6% of strain (red-shift). This analysis indicates that the optical threshold activity decreases to a lower value of photon energy by applying tensile strain. The equilibrium structure shows first three noticeable optical absorption peaks locating at 1.89 eV, 2.93 eV and 3.86 eV in VR region with absorbance up to 1.08×10^5 cm^{-1}. Similarly, Multiple higher absorption peaks at 6.11, 7.39, 14.26 eV with the absorbance up to 7.01×10^5 cm^{-1} (at 14.26 eV) are found in UV region. One can see that absorption peaks are more pronounced in the deep UV range as compare to VR. The exceptional long-range absorbance, from 1.69 eV to 20 eV, and multiple absorption peaks in UV and VR region indicate p-BCN as an appropriate light-harvesting material. The amplitude of these peaks slightly increases (decreases) with compressive (tensile) strain. While applying strain, these peaks slightly shift to higher energy values with reference to the equilibrium value. Further, there is no absorption of photon energy in the infrared (IR) region which indicates that the monolayer doesn't absorb heat at this range and can be operated in optical fibers and beam splitters[59].

Similarly, several reflectivity peaks are formed (Fig. 19) in both VR and UV regions, with very low intensity, for the strain-free monolayer. The maximum reflectivity is only
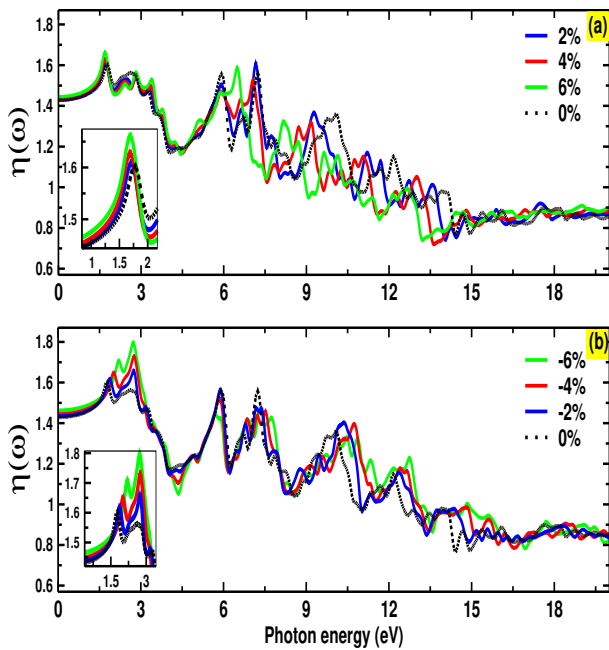
Figure 20: (Color online) Refractive index of p-BCN in tensile (a) and compressive (b) strain. The magnified view of the VR region is shown in the inset.

0.078 (at 7.33 eV) which is lower to that value of PG (0.12) [53]. Reflection spectra shows blue-shift (red-shift) with the growth in amplitude up to 0.096 (at 4%) by compressive (tensile) strain. Interestingly, the minor reflectivity peaks show that this monolayer becomes transparent in the energy range above 15 eV.

The refractive index $\eta(\omega)$ (Fig.20) describes the behavior of light propagating through the system. In particular, the value of the refractive index at zero photon energy gives the static refractive index $\eta(0)$. The value of $\eta(0)$ for p-BNC monolayer is 1.43 which is smaller than that value of penta-graphene(1.62) [56]. This value slightly increases and reaches up to 1.46 at 6% of compressive strain. Meanwhile, the value of the refractive index at the higher range of photon energy shows that the value is the highest (1.60) at 1.76 eV. The value of the refractive index reaches 1.79 (at 2.71 eV) at 6% of compressive strain.

Analyzing all the optical results, it is clear that the optical spectra are absent in the infrared region (IR) and they only appear around the UV and VR from 1.69 eV to 20 eV. The multiple peaks with greater amplitude show the p-BCN as an exceptional optical material that is operatable both in VR and UV regions. Especially, the high anisotropy and large optical absorption with lowest electron energy loss of monolayer indicate a high polarization sensitivity, and provide a good opportunity to design optical waveguide polarizers as well as energy harvesters.

4. Conclusions

In summary, we performed density functional theory (DFT) calculations, and predict that the pentagonal boron

carbon nitride (p-BCN) monolayer is structurally, dynamically, and mechanically stable direct bandgap semiconductor. The special quasi-sp^3 hybridized B−N and C−N bondings with unique geometry support the monolayer to possess intriguing chemical and physical properties. The biaxial strain creates significant structural reconstruction with shrinking and elongating bond lengths and angles, and thickness. The mechanical response is found very sensitive toward the strain. With the application of a small value of strain, a very rare negative Poisson's ratio (NPR), with hardening to softening, mechanical anisotropy to isotropy is detected. However, the monolayer is mechanically and dynamically unstable [32] at 6% of compression. Additionally, the bandgap is manipulated by loading the biaxial strain. Most importantly, our predictions on p-BCN show excellent optical response such as good static dielectric constant and refractive index, strong optical absorption (up to 1.08×10^5 cm^{-1} and 7.01×10^5 cm^{-1} in UV) with small energy loss and reflectance peaks both appearing in visible and ultraviolet regions (UV). The anisotropic geometry leads to acquiring strong optical anisotropy behavior in the monolayer. Although the optical response is not very sensitive toward the strain, the blue and red shift, with slight growth/reduction in spectral amplitude is noticed by tailoring with tensile and compressive strain. Hence, these exceptional physical and chemical properties exhibited by the p-BCN monolayer allow it to be a proper candidate material for nanomechanical and optoelectronic device applications.

5. Acknowledgment

References

[1] Andre Konstantin Geim. Graphene: status and prospects. *science*, 324(5934):1530–1534, 2009.

[2] Mengqi Zeng, Yao Xiao, Jinxin Liu, Kena Yang, and Lei Fu. Exploring two-dimensional materials toward the next-generation circuits: from monomer design to assembly control. *Chemical reviews*, 118 (13):6236–6296, 2018.

[3] C Kamal and Motohiko Ezawa. Arsenene: Two-dimensional buckled and puckered honeycomb arsenic systems. *Physical Review B*, 91(8): 085423, 2015.

[4] Deobrat Singh, Sanjeev K Gupta, Igor Lukačević, Matko Mužević, Yogesh Sonvane, and Rajeev Ahuja. Effect of electric field on optoelectronic properties of indiene monolayer for photoelectric nanodevices. *Scientific reports*, 9(1):1–12, 2019.

[5] Akinola D Oyedele, Shize Yang, Liangbo Liang, Alexander A Puretzky, Kai Wang, Jingjie Zhang, Peng Yu, Pushpa R Pudasaini, Avik W Ghosh, Zheng Liu, et al. Pdse2: pentagonal two-dimensional layers with high air stability for electronics. *Journal of the American Chemical Society*, 139(40):14090–14097, 2017.

[6] Geoffroy Prévot, Conor Hogan, Thomas Leoni, Romain Bernard, Eric Moyen, and Laurence Masson. Si nanoribbons on ag (110) studied by grazing-incidence x-ray diffraction, scanning tunneling microscopy, and density-functional theory: evidence of a pentamer chain structure. *Physical review letters*, 117(27):276102, 2016.

[7] Zhibin Gao, Zhaofu Zhang, Gang Liu, and Jian-Sheng Wang. Ultra-low lattice thermal conductivity of monolayer penta-silicene and penta-germanene. *Physical Chemistry Chemical Physics*, 21(47): 26033–26040, 2019.

[8] Mosayeb Naseri. Arsenic carbide monolayer: First principles prediction. *Applied Surface Science*, 423:566–570, 2017.

[9] Mosayeb Naseri, Jafar Jalilian, and AH Reshak. Electronic and optical properties of pentagonal-b2c monolayer: a first-principles calculation. *International Journal of Modern Physics B*, 31(8): 1750044, 2017.

[10] Shunhong Zhang, Jian Zhou, Qian Wang, and Puru Jena. Beyond graphitic carbon nitride: nitrogen-rich penta-cn2 sheet. *The Journal of Physical Chemistry C*, 120(7):3993–3998, 2016.

[11] Shunhong Zhang, Jian Zhou, Qian Wang, Xiaoshuang Chen, Yoshiyuki Kawazoe, and Puru Jena. Penta-graphene: A new carbon allotrope. *Proceedings of the National Academy of Sciences*, 112(8): 2372–2377, 2015.

[12] Shaoxiang Sheng, Runze Ma, Jiang-bin Wu, Wenbin Li, Longjuan Kong, Xin Cong, Duanyun Cao, Wenqi Hu, Jian Gou, Jun-Wei Luo, et al. The pentagonal nature of self-assembled silicon chains and magic clusters on ag (110). *Nano letters*, 18(5):2937–2942, 2018.

[13] Jorge I Cerdá, Jagoda Sławińska, Guy Le Lay, Antonela C Marele, José M Gómez-Rodríguez, and María E Dávila. Unveiling the pentagonal nature of perfectly aligned single-and double-strand si nano-ribbons on ag (110). *Nature communications*, 7(1):1–7, 2016.

[14] Akinola D Oyedele, Shize Yang, Liangbo Liang, Alexander A Puretzky, Kai Wang, Jingjie Zhang, Peng Yu, Pushpa R Pudasaini, Avik W Ghosh, Zheng Liu, et al. Pdse2: pentagonal two-dimensional layers with high air stability for electronics. *Journal of the American Chemical Society*, 139(40):14090–14097, 2017.

[15] Wai Leong Chow, Peng Yu, Fucai Liu, Jinhua Hong, Xingli Wang, Qingsheng Zeng, Chuang-Han Hsu, Chao Zhu, Jiadong Zhou, Xiaowei Wang, et al. High mobility 2d palladium diselenide field-effect transistors with tunable ambipolar characteristics. *Advanced Materials*, 29(21):1602969, 2017.

[16] Kexian Zhao, Yaguang Guo, Yiheng Shen, Qian Wang, Y Kawazoe, and Puru Jena. Penta-bcn: A new ternary pentagonal monolayer with intrinsic piezoelectricity. *The journal of physical chemistry letters*, 11(9):3501–3506, 2020.

[17] Thanasee Thanasarnsurapong, Klichchupong Dabsamut, Tosapol Maluangnont, Jiraroj T-Thienprasert, Sirichok Jungthawan, and Adisak Boonchun. Piezoelectric and electronic properties of hydrogenated penta-bcn: A computational study. *Journal of Applied Physics*, 129(9):095101, 2021.

[18] Jochen Heyd, Gustavo E Scuseria, and Matthias Ernzerhof. Hybrid functionals based on a screened coulomb potential. *The Journal of chemical physics*, 118(18):8207–8215, 2003.

[19] Safa Kasap and Peter Capper. *Springer handbook of electronic and photonic materials*. Springer, 2017.

[20] Zhaoyong Guan, Shuang Ni, and Shuanglin Hu. Tunable electronic and optical properties of monolayer and multilayer janus mosse as a photocatalyst for solar water splitting: a first-principles study. *The Journal of Physical Chemistry C*, 122(11):6209–6216, 2018.

[21] Dhara Raval, Bindiya Babariya, Sanjeev K Gupta, PN Gajjar, and Rajeev Ahuja. Ultrahigh carrier mobility and light-harvesting performance of 2d penta-pdx 2 monolayer. *Journal of Materials Science*, 56(5):3846–3860, 2021.

[22] José M Soler, Emilio Artacho, Julian D Gale, Alberto García, Javier Junquera, Pablo Ordejón, and Daniel Sánchez-Portal. The siesta method for ab initio order-n materials simulation. *Journal of Physics: Condensed Matter*, 14(11):2745, 2002.

[23] Emilio Artacho, Daniel Sánchez-Portal, Pablo Ordejón, Alberto García, and José M Soler. Linear-scaling ab-initio calculations for large and complex systems. *physica status solidi (b)*, 215(1):809–817, 1999.

[24] Norman Troullier and José Luís Martins. Efficient pseudopotentials for plane-wave calculations. *Physical review B*, 43(3):1993, 1991.

[25] John P Perdew, Kieron Burke, and Matthias Ernzerhof. Generalized gradient approximation made simple. *Physical review letters*, 77(18): 3865, 1996.

[26] Hendrik J Monkhorst and James D Pack. Special points for brillouin-zone integrations. *Physical review B*, 13(12):5188, 1976.

[27] Mohammad Noor-A-Alam, Hye Jung Kim, and Young-Han Shin. Dipolar polarization and piezoelectricity of a hexagonal boron nitride sheet decorated with hydrogen and fluorine. *Physical Chemistry Chemical Physics*, 16(14):6575–6582, 2014.

[28] Paolo Giannozzi, Stefano Baroni, Nicola Bonini, Matteo Calandra, Roberto Car, Carlo Cavazzoni, Davide Ceresoli, Guido L Chiarotti, Matteo Cococcioni, Ismaila Dabo, et al. Quantum espresso: a modular and open-source software project for quantum simulations of materials. *Journal of physics: Condensed matter*, 21(39):395502, 2009.

[29] Sonali Saha, TP Sinha, and Abhijit Mookerjee. Electronic structure, chemical bonding, and optical properties of paraelectric batio 3. *Physical Review B*, 62(13):8828, 2000.

[30] M Fadaie, N Shahtahmassebi, MR Roknabad, and O Gulseren. Investigation of new two-dimensional materials derived from stanene. *Computational Materials Science*, 137:208–214, 2017.

[31] Mohammad Ali Mohebpour, Sahar Izadi Vishkayi, and Meysam Bagheri Tagani. Tuning electronic and optical properties of free-standing sn2bi monolayer stabilized by hydrogenation. *Journal of Applied Physics*, 127(1):014302, 2020.

[32] Klichchupong Dabsamut, Thanasee Thanasarnsurapong, Tosapol Maluangnont, T Jiraroj, Sirichok Jungthawan, Adisak Boonchun, et al. Strain engineering and thermal conductivity of a penta-bcn monolayer: a computational study. *Journal of Physics D: Applied Physics*, 2021.

[33] Shambhu Bhandari Sharma, Ramchandra Bhatta, Keshav Raj Sigdel, Rajendra P Adhikari, and Gopi Chandra Kaphle. Structural, electronic, magnetic and mechanical properties of vanadium-doped boron nitride monolayer. *The European Physical Journal B*, 94(6):1–7, 2021.

[34] Fengyu Li, Kaixiong Tu, Haijun Zhang, and Zhongfang Chen. Flexible structural and electronic properties of a pentagonal b 2 c monolayer via external strain: a computational investigation. *Physical Chemistry Chemical Physics*, 17(37):24151–24156, 2015.

[35] Jiao Li, Xinyu Fan, Yanpei Wei, Haiying Liu, Shujuan Li, Peng Zhao, and Gang Chen. Half-metallicity and ferromagnetism in penta-aln 2 nanostructure. *Scientific reports*, 6(1):1–10, 2016.

[36] Yi Ding and Yanli Wang. Hydrogen-induced stabilization and tunable electronic structures of penta-silicene: a computational study. *Journal of Materials Chemistry C*, 3(43):11341–11348, 2015.

[37] Shijie Liu, Bo Liu, Xuhan Shi, Jiayin Lv, Shifeng Niu, Mingguang Yao, Quanjun Li, Ran Liu, Tian Cui, and Bingbing Liu. Two-dimensional penta-bp 5 sheets: High-stability, strain-tunable electronic structure and excellent mechanical properties. *Scientific reports*, 7(1):1–8, 2017.

[38] Li Shao, Yan Li, Qingxin Yuan, Mingyu Li, Yinxiao Du, Fanguang Zeng, Pei Ding, and Honggang Ye. Effects of strain on mechanical and electronic properties of borophene. *Materials Research Express*, 4(4):045020, 2017.

[39] Yvon Le Page and Paul Saxe. Symmetry-general least-squares extraction of elastic data for strained materials from ab initio calculations of stress. *Physical Review B*, 65(10):104104, 2002.

[40] Max Born and Rama Dhar Misra. On the stability of crystal lattices. iv. In *Mathematical Proceedings of the Cambridge Philosophical Society*, volume 36, pages 466–478. Cambridge University Press, 1940.

[41] Ruishan Li, Qian Shao, Enlai Gao, and Ze Liu. Elastic anisotropy measure for two-dimensional crystals. *Extreme Mechanics Letters*, 34:100615, 2020.

[42] Shivakumar I Ranganathan and Martin Ostoja-Starzewski. Universal elastic anisotropy index. *Physical review letters*, 101(5):055504, 2008.

[43] Christopher M Kube and Maarten De Jong. Elastic constants of polycrystals with generally anisotropic crystals. *Journal of Applied Physics*, 120(16):165105, 2016.

[44] Shao-Bo Chen, Zhao-Yi Zeng, Xiang-Rong Chen, and Xing-Xing Yao. Strain-induced electronic structures, mechanical anisotropy, and piezoelectricity of transition-metal dichalcogenide monolayer crs2. *Journal of Applied Physics*, 128(12):125111, 2020.

[45] Guoxin Cao. Atomistic studies of mechanical properties of graphene. *Polymers*, 6(9):2404–2432, 2014.

[46] Ruhao Fang, Xiangyuan Cui, Catherine Stampfl, Simon P Ringer, and Rongkun Zheng. Negative poisson's ratio in 2d life-boat structured crystals. *Nanoscale Advances*, 1(3):1117–1123, 2019.

[47] George Neville Greaves, AL Greer, Roderic S Lakes, and Tanguy Rouxel. Poisson's ratio and modern materials. *Nature materials*, 10 (11):823–837, 2011.

[48] Akhtar Hussain, Hafiz Muhammad Rafique, Muhammad Tayyab, et al. Computational study of be-doped hexagonal boron nitride (h-bn): Structural and electronic properties. *Computational Condensed Matter*, 23:e00474, 2020.

[49] Su-Huai Wei and Alex Zunger. Predicted band-gap pressure coefficients of all diamond and zinc-blende semiconductors: Chemical trends. *Physical Review B*, 60(8):5404, 1999.

[50] Tie-Yu Lü, Xia-Xia Liao, Hui-Qiong Wang, and Jin-Cheng Zheng. Tuning the indirect–direct band gap transition of sic, gec and snc monolayer in a graphene-like honeycomb structure by strain engineering: a quasiparticle gw study. *Journal of Materials Chemistry*, 22(19):10062–10068, 2012.

[51] S Bhandari Sharma, Rajendra Adhikari, Keshav Raj Sigdel, and Ramchandra Bhatta. Strain induced electronic and optical properties of 2d silicon carbide monolayer using density functional theory. *Journal of Nepal Physical Society*, 7(1):60–65, 2021.

[52] Juan Du, Peng Song, Lizhen Fang, Tianxing Wang, Zhongming Wei, Jingbo Li, and Congxin Xia. Elastic, electronic and optical properties of the two-dimensional ptx2 (x= s, se, and te) monolayer. *Applied Surface Science*, 435:476–482, 2018.

[53] XS Dai, T Shen, Y Feng, and HC Liu. Structure, electronic and optical properties of al, si, p doped penta-graphene: A first-principles study. *Physica B: Condensed Matter*, 574:411660, 2019.

[54] Rita John and Benita Merlin. Optical properties of graphene, silicene, germanene, and stanene from ir to far uv–a first principles study. *Journal of Physics and Chemistry of Solids*, 110:307–315, 2017.

[55] Akash Laturia, Maarten L Van de Put, and William G Vandenberghe. Dielectric properties of hexagonal boron nitride and transition metal dichalcogenides: from monolayer to bulk. *npj 2D Materials and Applications*, 2(1):1–7, 2018.

[56] Zhanyu Wang, F Dong, Bo Shen, RJ Zhang, YX Zheng, LY Chen, SY Wang, CZ Wang, KM Ho, Yuan-Jia Fan, et al. Electronic and optical properties of novel carbon allotropes. *Carbon*, 101:77–85, 2016.

[57] F Lahourpour, A Boochani, SS Parhizgar, and SM Elahi. Structural, electronic and optical properties of graphene-like nano-layers mox2 (x: S, se, te): Dft study. *Journal of Theoretical and Applied Physics*, 13(3):191–201, 2019.

[58] Akshay M Satawara, Gaushiya A Shaikh, Sanjeev K Gupta, and PN Gajjar. Structural, electronic and optical properties of hexagonal boron-nitride (h-bn) monolayer: An ab-initio study. *Materials Today: Proceedings*, 2020.

[59] Hamad Rahman Jappor and Majeed Ali Habeeb. Optical properties of two-dimensional gas and gase monolayers. *Physica E: Low-dimensional Systems and Nanostructures*, 101:251–255, 2018.